Results in Physics 15 (2019) 102683

Contents lists available at ScienceDirect

Results in Physics

journal homepage: www.elsevier.com/locate/rinp

Magnetic phase transition of mechanically alloyed single sample $Co_{0.5}Ni_{0.5}Fe_2O_4$

Zhi Huang Low[a], Ismayadi Ismail[a,*], Mohd Shamsul Ezzad Shafie[a], Idza Riati Ibrahim[a], Mehmet Ertuğrul[b], Rabaah Syahidah Azis[a], Norlaily Mohd Saiden[a], Intan Helina Hasan[a], Fadzidah Mohd Idris[c], Rodziah Nazlan[d]

[a] Institute of Advanced Technology, Universiti Putra Malaysia, 43400 Serdang, Selangor Darul Ehsan, Malaysia
[b] Engineering Faculty, Ataturk University, 25240 Erzurum, Turkey
[c] PERMATA Insan College, Universiti Sains Islam Malaysia, PERMATA Insan Complex, Bandar Baru Nilai, 71800 Nilai, Negeri Sembilan, Malaysia
[d] Department of Materials Technology, Faculty of Industrial Science and Technology, Universiti Malaysia Pahang, Kampus Gambang, Lebuhraya Tun Razak, Kuantan, Pahang, Malaysia

ARTICLE INFO

Keywords:
$Co_{0.5}Ni_{0.5}Fe_2O_4$
Microstructural evolution
Activation energy
Magnetic transition

ABSTRACT

The parallel evolutional relationship between microstructural properties and magnetic and electrical properties was elucidated through this study. A $Co_{0.5}Ni_{0.5}Fe_2O_4$ rod sample was prepared via high energy ball milling and subsequent moulding into a nano-sized compacted powder. This single sample was sintered through 10 cycles at different sintering temperatures in the range of 500 °C–1400 °C. After each sintering, the sample was characterized for its phase, microstructural, density, magnetic and electrical properties using XRD, SEM, B-H tracer, Curie temperature measurement and two probes method. An integrated study of microstructural properties with elevating sintering temperature would point to the existence of three stages of sintering, which involved atomic, interfaces (lattice and boundaries), and volume diffusions respectively. Three distinct shape-differentiated groups of B–H hysteresis loops were observed. The existence of these groups was associated with microstructural properties such as phase purity, volume fraction of disordered phase or grain boundaries, and grain size. In terms of average grain size, from 48.25 nm to 71.93 nm, a weak paramagnetic behaviour was observed; while from 83.65 nm to 374.79 nm, a relatively square-shaped hysteresis loops with moderate ferromagnetic behaviours were observed. The occurrences of erect and well-defined sigmoid-shape were observable when there were sufficiently high single-phase purity and crystallinity, where the average grain size was in the range of 964.73 nm–11215.91 nm. The critical grain size of 186.75 nm was found by plotting average grain size against coercivity, suggesting the number of single-domain particles was reduced, and the number of multi-domain particles was increased by increasing sintering temperature. The electrical resistivity variations were strongly related to the microstructural properties.

Introduction

Ferrites are among the most widely used groups of magnetic ceramics in engineering products. The behaviours of polycrystalline ferrites are strongly related to chemical compositions, microstructure, and crystal structure. The remarkable magnetic properties of spinel ferrites originate from the interactions between cations with resultant magnetic moments that are situated in the tetrahedral and octahedral sites [1]. Nickel ferrite and cobalt ferrite both possess an inverse spinel structure, where iron cations are distributed equally in tetrahedral and octahedral sites, while the other constituent cations (nickel, cobalt) are mainly in octahedral sites [2,3]. Nickel and cobalt ferrites have attracted increasing attention and have been considered for applications such as magnetic sensors, wave absorbers, telecommunications, and magnetic composites. Nickel ferrite is a soft ferrite with high magnetocrystalline isotropy while maintaining high resistivity. On the other hand, cobalt ferrite is a hard ferrite with high magneto-crystalline anisotropy, high coercivity, and moderate saturation magnetization, while possessing high chemical and mechanical stability. Therefore, cobalt nickel ferrite, $Co_{0.5}Ni_{0.5}Fe_2O_4$ possesses high electrical resistivity and unique magnetic properties suitable for high-frequency electronic applications, electrodes for supercapacitors, microwave devices, chemical sensors,

* Corresponding author.
E-mail address: ismayadi@upm.edu.my (I. Ismail).

https://doi.org/10.1016/j.rinp.2019.102683
Received 26 July 2019; Received in revised form 17 September 2019; Accepted 17 September 2019
Available online 20 September 2019

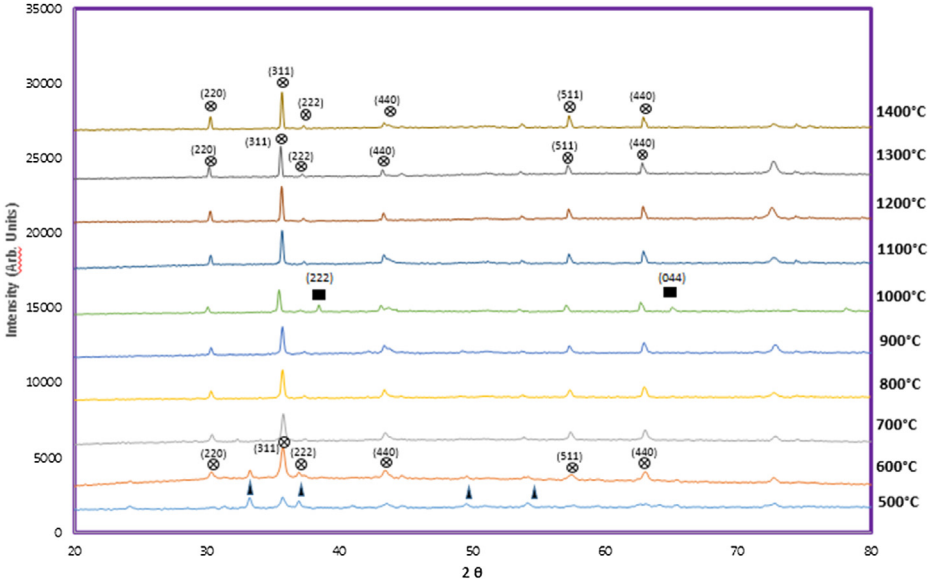

Fig. 1. XRD graph of SSS $Co_{0.5}Ni_{0.5}Fe_2O_4$ after sintering from 500 °C to 1400 °C. ▲ = Fe_2O_3, ⊕ = $Co_{0.5}Ni_{0.5}Fe_2O_4$, ■ = Co_2O_4.

information storage, and electronic chips [4–8].

Studies have shown that heat treatment, such as sintering can be utilised for controlling the microstructural properties of polycrystalline ferrites, particularly grain size, porosity, and grain boundaries [9–12]. The objective of this work, with the combination of High Energy Ball Milling (HEBM), is a systematic study on the correlations between magnetic and electrical behaviours, with microstructural properties of $Co_{0.5}Zn_{0.5}Fe_2O_4$. Compared to conventional solid-state route, pre-treated powder with HEBM has an advantage of mechanical activation of particles; hence, the formation of polycrystalline ferrites can be obtained at a relatively low sintering temperature. Additionally, an experimental sequence focused on the property-microstructure relationships will be carried out on a single sample throughout a series of ascending sintering temperature (Single Sample Sintering (SSS) technique). Therefore, thermal history may come into the picture of systematically tracking the property-microstructure relationships, providing a higher consistency and reliability in the fundamental line of scientific inquiry.

Materials and methods

All raw powders were purchased from Alfa Aesar without any further purification. The starting raw powders consisted of Co_3O_4 (97.7%), Fe_2O_3 (99.5%), and NiO (99.0%) with molar mass of 240.8 g/mol, 159.69 g/mol and 74.6928 g/mol respectively. The starting powders were weighed according to the stoichiometric ratio of Co_3O_4:NiO:Fe_2O_3 to be 1:3:6 based on a molar ratio. Then, the powders were milled using SPEX 8000D, in a hardened steel vial. A ball to powder ratio of 10:1 was chosen. The high energy ball milling was carried out for 6 h, accompanied by ten hardened steel balls, with each ball of 12 mm in diameter. The rotational speed of the vials was fixed at 1450 rpm. The as-milled powder was blended with 1 to 2 wt% of polyvinyl alcohol to obtain a granulated powder. A hydraulic pressing machine was used to press at 300 MPa to obtain a rod sample. The rod formed with the size of 20 mm in diameter and 10 mm in height. Optimisation of the milling process and making rod sample was already reported elsewhere [13–15]. The rod sample was then sintered repeatedly for 10 cycles in air at different sintering temperatures of 500 °C, 600 °C, 700 °C, 800 °C, 900 °C, 1000 °C, 1100 °C, 1200 °C, 1300 °C, and 1400 °C for 10 h. After every cycle, the sample was examined. Phase evaluation was carried out with Philips X'PERT diffractometer. The evaluation was accomplished using filtered Cu Kα radiation (l = 0.1542 nm) obtained in the 2θ range of 20 to 80° using a scan step of (2θ) = 0.033 with 5 s per step as the counting. The topographical and morphological observations were obtained using a Nova NanoSEM 50 scanning electron microscope. An intercept method of over 200 grains was used using ImageJ software to measure the grain size. The Archimedes principle with water as the fluid medium was used to measure the density of the toroidal bulk sample. The percentage theoretical density (%D_{th}) was calculated using the following formula:

$$\%D_{th} = (\text{measured density/theoretical density}) \times 100\% \quad (1)$$

The theoretical density of $Ni_{0.5}Co_{0.5}Fe_2O_4$ was calculated by taking the molecular weight of $Ni_{0.5}Co_{0.5}Fe_2O_4$ to be 234.51 g. The weight of 8 molecules in 1 unit cell is (8)×237.73/A, where A is Avogadro's number. The volume of a cube of side length a is a^3. The unit cell edge a_o (Å) of $Ni_{0.5}Co_{0.5}Fe_2O_4$ = 8.360Å therefore a^3 = 584 Å^3. As 1Å^3 = 10^{-24}cm^3, theoretical density is mass/volume equal to $\left[(8) \times \frac{234.51}{6.022 \times 10^{23}}\right]/584 \times 10^{-24}$, which is equal to 5.335 g/cm^3.

The theoretical density, ρ_x, was calculated as above. The percentage of porosity, P, of the sample was calculated using the relation below:

$$P = \left[1 - \frac{\rho}{\rho_x}\right] \times 100\% \quad (2)$$

where ρ is the measured density of the sample.

The B–H hysteresis loops of the bulk samples were studied, and the magnetic properties were extracted using a MATS-2010SD Static Hysteresisgraph. The electrical resistivity was measured using two probes method. Curie temperature was measured using a method involving sample wounded with copper wire, placed in a furnace and heated up to 300 °C. The inductance values were obtained using an HP4294A Precision Impedance Analyzer. The Curie Temperature values were determined by plotting graphs of initial permeability against temperature.

Results and discussions

Phase and microstructural analysis

The X-ray diffraction patterns of SSS $Co_{0.5}Ni_{0.5}Fe_2O_4$ (Simple Sample Sintering cobalt nickel ferrite) from 500 to 1400 °C are displayed in Fig. 1. The Bragg diffraction angles (2θ) of all the peaks were identified individually according to the reference of ICDD. Samples

sintered at 500 °C show a trace of α-Fe_2O_3 (ICCD: 01-079-1741), Co_3O_4 (ICCD: 01-078-0429 and 01-076-1802) and a small trace of $Ni_{1.25}Fe_{1.85}O_4$ (ICCD: 01-088-0380). This result shows that partial diffusion had occurred at 500 °C. When sintering temperature was increased from 700 to 1400 °C, $CoFe_2O_4$ (ICCD: 00-027-1029) and $NiFe_2O_4$ (ICCD: 00-032-0072) phases diffused, and a $Co_{0.5}Ni_{0.5}Fe_2O_4$ phase occurred [16–18]. It is worth mentioning that the SSS method influences the volume fractions of different phases in the diffraction patterns. Due to the existence of the thermal history of SSS, the volume fractions of phases disappear with only the visibility of a single sharp peak. The $Co_{0.5}Ni_{0.5}Fe_2O_4$ phase formed at a relatively lower sintering temperature (700 °C) compared to the conventional solid-state process due to the mechanical activation of the constituents with high energy ball milling before sintering. The mechanical activation allows the formation of polymorphic iron oxide phases, and diffusion mechanism can take place at low sintering temperatures. Interestingly, there existence of peaks at 38° with (2 2 2) peak and at 65° with (0 4 4) peak for sample sintered at 1000 °C, contributed by intermediate species which is cobalt (III) oxide. Beside these peaks, there is also another peak showing an intermediate phase which is nickel iron oxide, existed at 73° with (3 3 5) peak. These peaks clearly show that there are intermediate phases of cobalt (III) oxide and nickel iron oxide co-existed together. Beyond the 70°, there are some relatively low intensity peaks, consist of (0 2 6), (2 2 6), which is not significant to mention as they are not the main peaks [19].

The strain (ε) and the average crystallite size (D_{XRD}) were estimated using the Williamson-Hall method (Eq. (3)).

$$\beta cos\theta = \frac{0.9\lambda}{D} + 4.\ \varepsilon.\ sin\theta \tag{3}$$

where λ is the wavelength of CuKα radiation (1.5406 Å), β is the broadening of full width at half the maximum intensity (FWHM), hkl are the Miller indices, θ is the Bragg angle (o).

The lattice constant, a (Å) was calculated from Bragg's law with Nelson-Riley correction (Eq. (4)) [20,21].

$$\alpha = \frac{\lambda\sqrt{h^2 + k^2 + l^2}}{2sin\theta} \tag{4}$$

where λ is the wavelength of CuKα radiation (1.5406 Å), hkl are the Miller indices, θ is the Bragg angle (o).

Table 1 shows the structural and physical properties extracted from XRD results. There was a drastic decrease in lattice parameter *a* after 500 °C, which is believed to have resulted from the mechanically induced oxygen vacancies in the structure and disrupted the super-exchange (A–O–B) bonds [22]. As a result, relatively smaller Ni^{2+} ions, with an ionic radius of 0.78 Å, were diffused into the voids at lower sintering temperatures. HEBM induces three phenomena: (i) The contraction of lattice space of ferrite as the milling time increased; (ii) the crystal lattice grew with a considerable amount of voids; and (iii) the redistribution of cations from its ordinary tetrahedral and octahedral sites [23]. The lattice parameter varies with increasing milling time as the result of an accumulation of lattice strain [24]. The variation of lattice parameters highlights that there were changes in the ratio of Fe^{3+} cations in octahedral and tetrahedral, which is caused by the introduction of Ni^{2+}. The original cation distribution was disrupted by the Ni^{2+} cations, as Co^{2+} ions were forced to the tetrahedral sites due to the selective transfer of Co^{2+} because of its larger size (0.745 Å) compared to Fe^{3+} ions (0.645 Å); while some Fe^{3+} ions were forced into the octahedral sites to release the strain from the introduction of Ni^{2+} ions [1].

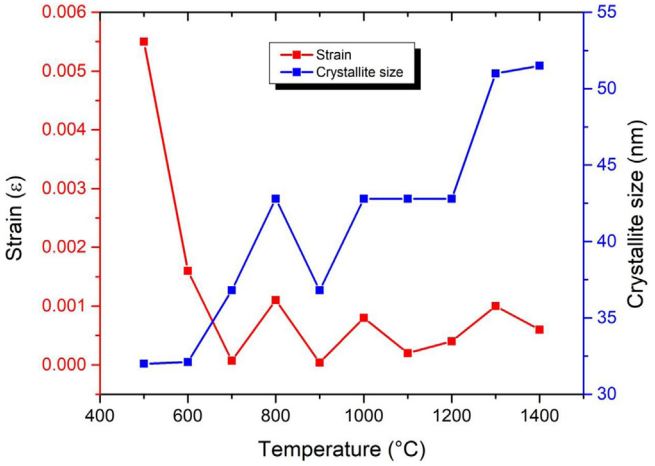

Fig. 2. Strain and crystallite size variations of SSS $Co_{0.5}Ni_{0.5}Fe_2O_4$ with sintering temperature from 500 °C to 1400 °C.

The lattice strain and crystallite size of SSS $Co_{0.5}Ni_{0.5}Fe_2O_4$ were calculated by Williamson-Hall analysis by assuming the strain is uniform in all crystallographic directions [25]. Fig. 2 shows the strain and crystallite size variations of SSS $Co_{0.5}Ni_{0.5}Fe_2O_4$ with sintering temperature from 500 °C to 1400 °C. The lattice strain decreases from 500 to 700 °C and fluctuates within a range between 40 and 1100 microstrain from 700 to 1400 °C. This is thought to be due to the thermal history of a single sample sintering method. One sample was used for different sintering temperatures; therefore the sensitivity to thermal treatment decreases after each thermal treatment. The crystallite size also increases with the increasing of sintering temperatures. This indicates that the increase in crystallization reaction caused the material to possess a greater degree of magnetocrystalline anisotropy and exchange interaction that determine the direction in which magnetization prefers to be oriented [26].

The as-milled sample has a nanocrystalline structure, and it is thermodynamically unstable with high spontaneous strain. Sintering at 500, 600, and 700 °C had caused the lattice strain relaxation by removing the oxygen vacancies at grain boundaries as mentioned before. There was a higher level of lattice strain relaxation and structural phase

Table 1
Lattice parameters, Density, theoretical density, porosity and phases of SSS $Co_{0.5}Ni_{0.5}Fe_2O_4$ samples sintered from 500 °C to 1400 °C.

T_s (°C)	Lattice Parameter		Experimental Density (g/cm^3)	Theoretical density (%)	Porosity (%)	Phase
	a (Å)	V_O (Å^3)				
500	10.36	1114.15	4.721	88	12	Fe_2O_3, Co_3O_4, $Ni_{1.25}Fe_{1.85}O_4$
600	8.33	579.37	4.770	89	11	Fe_2O_3, $CoFe_2O_4$, $NiFe_2O_4$
700	8.32	577.94	4.799	90	10	$Co_{0.5}Ni_{0.5}Fe_2O_4$
800	8.34	580.41	4.818	90	10	$Co_{0.5}Ni_{0.5}Fe_2O_4$
900	8.34	580.76	4.847	91	9	$Co_{0.5}Ni_{0.5}Fe_2O_4$
1000	8.4	593.03	4.875	91	9	$Co_{0.5}Ni_{0.5}Fe_2O_4$
1100	8.35	582.21	4.895	92	8	$Co_{0.5}Ni_{0.5}Fe_2O_4$
1200	8.35	583.52	4.931	92	8	$Co_{0.5}Ni_{0.5}Fe_2O_4$
1300	8.37	586.96	4.962	93	7	$Co_{0.5}Ni_{0.5}Fe_2O_4$
1400	8.35	582.55	4.952	93	7	$Co_{0.5}Ni_{0.5}Fe_2O_4$

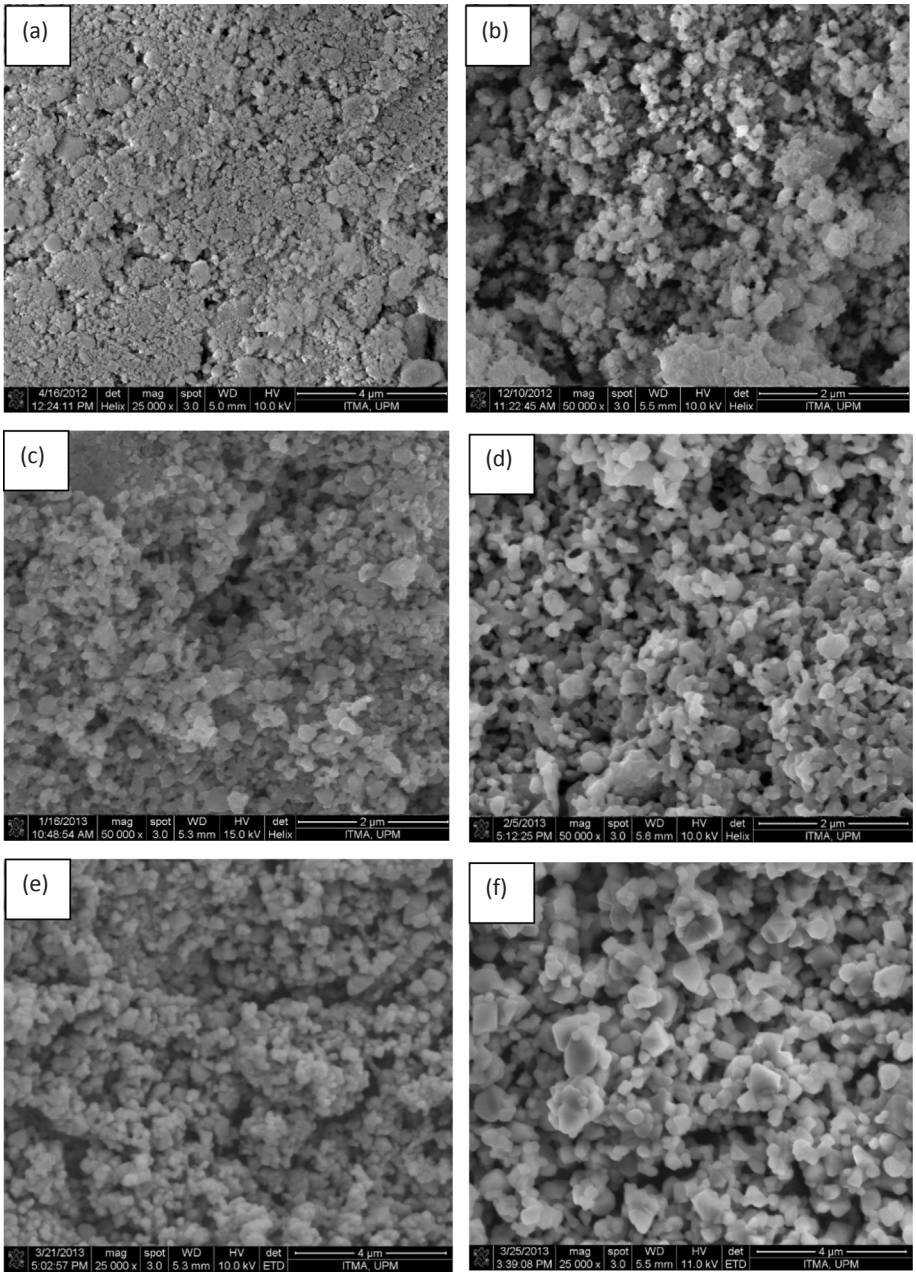

Fig. 3. FeSEM images of a mechanically activated $Co_{0.5}Zn_{0.5}Fe_2O_4$ sample sintered at: (a) 500 °C, (b) 600 °C, (c) 700 °C, (d) 800 °C, (e) 900 °C, (f) 1000 °C, (e) 1100 °C, (f) 1200 °C, (g) 1300 °C, and (i) 1400 °C.

transition, which reduced the total energy of the system [2]. The trend of the lattice for the thermal treatments above 700 °C supports the thermal history argument of the SSS method. After several heat treatments, the sample achieved higher thermal stability. The disordering effect of HEBM was reduced after SSS indicates that instead of overcoming the crystal defects, the thermal energy was used entirely for boundary and volume diffusion. Grain growth and densification were observed for heat treatments above 700 °C [27]. On the other hand, the reduction of lattice strain could associate with the increase of crystallite size with the increase of sintering temperature.

In view of the FESEM micrographs obtained, three stages of sintering are shown in Fig. 3. The average grain size with the respective sintering temperature is presented in Fig. 4. It can be observed that after high energy ball milling, the grain size became nano-sized (48.25 nm) due to ball-to-ball and vial-to-ball collisions. 6 h of milling may produce enough heat energy for agglomeration. It is apparent that during the early stage of sintering, there were formations of dumb-bell structure or necking structures that were formed between grains. These structures were formed to enable material transport mechanisms. Obviously during the early stage, viscous flow and material transport from grain boundary are the mechanisms involved in the reduction of interparticle distance. The interparticle distance is reduced until the distance is close enough for the formation of a necking structure. The neck size increased at this stage is due to material transport from the grain boundary to this neck structure without changing its interparticle distance [27]. Therefore, at this stage, grain boundaries are the primary source of material transport. In the early stage, grain growth is limited. However, a slight coarsening of the microstructure is expected due to surface diffusion.

It is found that the average grain size (Fig. 4) increases slowly and almost linearly from the early stage until the intermediate stage of sintering. However, it increases rapidly at the final stage of sintering indicating that there is a significance of densification with minimal

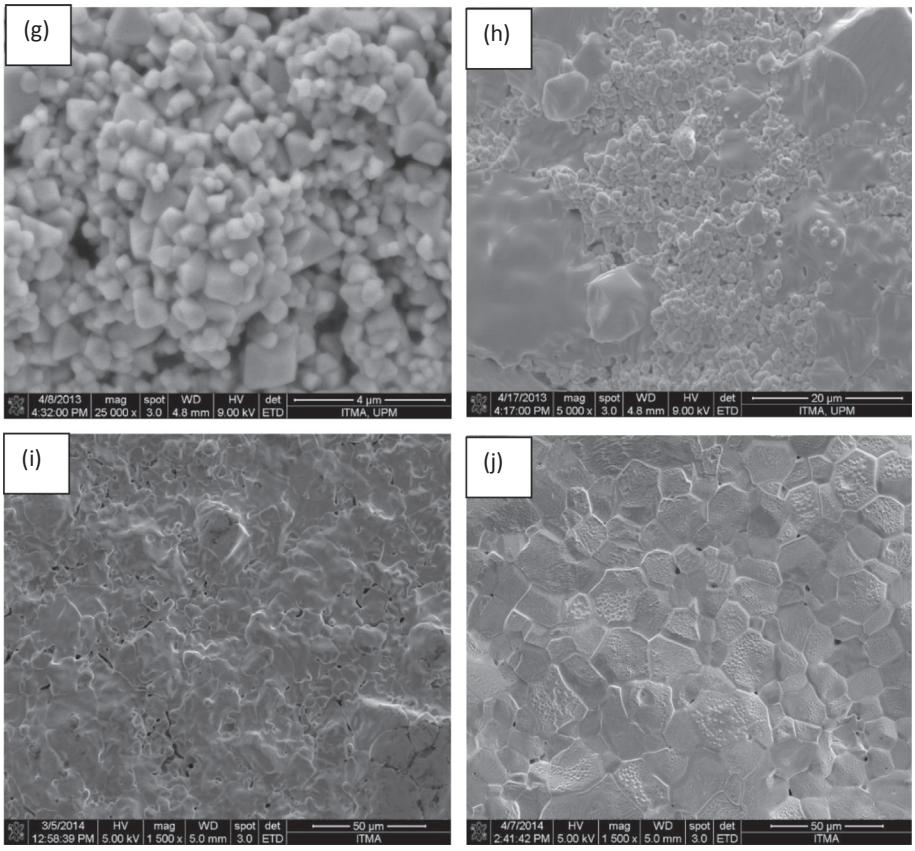

Fig. 3. (*continued*)

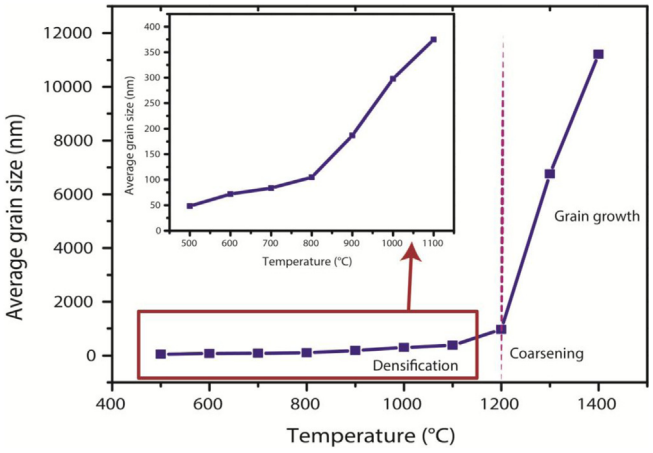

Fig. 4. Variation of average grain size of a mechanically activated $Co_{0.5}Zn_{0.5}Fe_2O_4$ sample sintered at different sintering temperature ranging from 500 °C to 1400 °C.

grain growth stage, followed by another stage of minimal densification but significant grain growth [28]. From Fig. 3, the micrographs at intermediate stages show the coalescence of pores and the increase of pore size, suggesting that there were migrations of boundaries during this stage. Afterward, the transition of the continuous pore network to isolated and closed pores highlights the transition from intermediate to the final stage of sintering. It is worth mentioning that the transitions from early, to intermediate, and the final stage of sintering, produce a more homogenous microstructure. The porosity seems to linearly decrease with increasing sintering temperature (Table 1). It is common in powder processing where the porosity during the sintering decreased by mass transport through lattice diffusion with grain growth [29]. However in the final stage of sintering at 1400 °C, abnormal grain growth can be observed because of the porosity network loses stability, forming closed spherical or ellipsoidal pores, which are located in triple junctions. At this temperature, microstructure would affect much in magnetic properties.

The activation energy of grain growth can be calculated using the Arrhenius equation and Coble's theory as reported previously in refs. [10,30,31] using this equation:

$$\log D = -Q/2.303R\left(\frac{1}{T}\right) + A \tag{5}$$

where D, Q, R, T, A are the average grain size, activation energy, ideal gas constant, temperature and a constant, respectively. Fig. 5 shows that when calculating the activation energy (Q) based on Arrhenius Eq. (5), three stages of sintering were predominantly observed as predicted. The activation energies calculated from the Arrhenius equation are

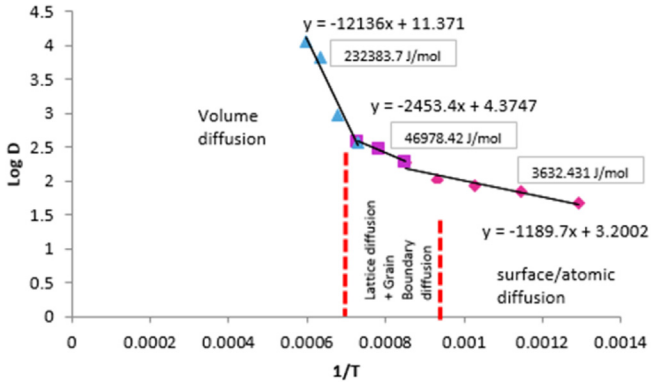

Fig. 5. Plots of log *D* versus the reciprocal of absolute temperature (1/*T*) for SSS $Co_{0.5}Ni_{0.5}Fe_2O_4$.

3.63 kJ/mol (Group 1), 46.9 kJ/mol (Group 2) and 232 kJ/mol (Group 3), respectively which represents the increase of activation energy as the result of a decrease in surface area. This phenomenon is associated with the Scott equation, where the decrease in surface area of the sintered samples is due to the increase in grain size by sintering [2]. When the average grain size was relatively small (500 °C to 1400 °C), the surface area was relatively large. As the results, the lower activation energy is required for surface and atomic diffusions to pre-dominate the material transport mechanism. During the intermediate stage, the coarsening of grains reduced the surface area, resulted in lesser surface area for the reaction to occur, causing the increase of activation energy. This is when the lattice and grain boundary diffusion dominated. Finally, in the final stage, the dominance of volume diffusion can be explained by the rapid reduction of surface area due to the large average grain size.

Magnetic properties analysis

Variation of magnetic behaviours of single sample sintering of $Co_{0.5}Ni_{0.5}Fe_2O_4$ with an increase in the sintering temperature was studied with B-H hysteresis tracer. Plotted B-H hysteresis loop curves for different sintering temperatures ranging from 500 °C to 1400 °C are shown in Fig. 6. Previous studies showed that grain size plays a crucial role in determining the hysteresis loop shape [32,33].

According to the shape of hysteresis loops, the magnetic behaviours of the sintered single sample were divided into three distinctive shapes (Fig. 6b). The hysteresis loops of sintering temperature 500 °C and 600 °C are categorised as group 1 due to their shapes that are nearly linear, and the coercivity values (H_c) are almost zero. It reveals the existence of paramagnetic (amorphous phase) and superparamagnetic phases (crystalline phase) which could be attributed to the hematite phase that existed at this stage. Although paramagnetic and superparamagnetic phases were co-existed, the low induction magnetization (B_s) of 2.38 emu/g and 5.31 emu/g for sintering at 500 and 600 °C respectively suggesting that there was only a small amount of crystalline phase. The atoms in the grain boundary are believed to be randomly arranged (amorphous phase), of which these are the inactive magnetic layer, and the atoms within boundary or core atoms are believed to be orderly arranged (crystalline phase). At 500 °C and 600 °C, the average grain size of the sample was in the nano-size region. Therefore, the number of atoms in the boundary will be in the same order as the number of core atoms [12]. As a result, the volume fraction of the amorphous phase was comparable with the volume fraction of the crystalline phase, and it dominated the magnetic behaviour of the material.

Given the variations of B_s values as a function of sintering temperature, it is noted that sintering of 700, 800, 900, 1000, and 1100 °C increased the B_s values from 23.98 emu/g to 101.37 emu/g. The trend is consistent with Fig. 1, where the increase of sintering temperature increases the ferromagnetic crystalline phase in the sample. The second group is categorised by the square-shaped hysteresis loops. As a result, the BH_{max} values of this group are in the same order, as shown in Table 2 signifies the energy stored in the sample after a cycle of magnetization and demagnetization is most significant for this group. The magnetic behaviours of the sample at sintering temperature of 1200, 1300, and 1400 °C are categorised as Group 3, of which the erect, narrower, and well-defined sigmoid shapes were observed. B_s values continued to increase and maxed out at 109.78 emu/g during 1300 °C, and reduced to 99.07 emu/g at 1400 °C. At this point, the average grain size of the samples are in the micron region, and the volume fraction of disorder, amorphous phase in the grain boundaries is not significant. The repeated high thermal treatments on a single sample however have introduced intergranular pores at 1400 °C (Fig. 3), and the defects reduced the B_s value.

Fig. 7 shows that the H_c values increased with sintering of sample sintered from 500 to 900 °C, reached a maximum value of 0.55 kOe, followed by a decrease from 900 to 1400 °C. The turning point is known as critical size (D_c), where there is a transition from a single domain region to a multi-domain region which can be explained with extrinsic related properties like porosity and grain size [12].

The increasing coercivity of a single domain region indicates that there is a larger magnetic field required to change the direction of the magnetic moments as the sintering temperature was increased from 500 to 900 °C. As the size is relatively small (< Dc), grain boundaries are significant in terms of volume fraction; they are blocking the interaction between particles. Therefore, single domain particles are dominant as the magnetic moment of all individual particles is randomly oriented. As the crystallinity increases with increasing sintering temperature, the spontaneous magnetization of individual particle increases while maintaining single domain formation. Therefore, coercivity increases with the average particle size. With further increase of particle size (> Dc), the influence of amorphous phase diminishes; and the exchange interaction between particles is now permitted. This activates the creation of domain walls. Therefore, the required external field to change the orientation of moments decreases, and the coercivity decreases [34–38].

At lower sintering temperature from 500 to 700 °C, the null value of Curie temperature was observed and it is in agreement with B-H hysteresis results where the paramagnetic phase was dominant at this stage. After 900 °C, the Curie temperature was observed at a range of 450 to 650 °C. From the previous study [33], the Curie temperature of cobalt zinc ferrite was observed at approximately 180 °C. In the case of the single sample sintering method, thermal history could affect compositional homogeneity and the possible presence of stable phases. The thermal equilibrium during the heating and cooling process could affect the site occupancy of Co, Ni, and Fe among the A and B sites, thereby affecting the strength of the exchange interactions. On the other hand, magnetic ion substitution will sustain the superexchange interaction, which leads to an increase of Curie temperature.

Electrical properties analysis

The variation of room temperature electrical resistivity with increasing sintering temperature is plotted in Fig. 8. It is apparent that electrical resistivity decreased with increasing sintering temperature from 500 to 900 °C and can be associated with the small grain size during this stage. It is known that small grain size possesses a higher surface area and a more significant number of grain boundaries [39]. The high number of grain boundaries provides a greater number of energy mismatch between each energy stage of neighboring grains. These areas act as obstacles for the electron to flow [40]. As the average grain size increases with increasing sintering temperature, the homogeneity increases. Thus, the obstacle for electrons flow diminishes, and resistivity decreases. The increase of resistivity from 900 to 1400 °C is attributed to porosity. Pores contribute to charge vacancies, and they act as scattering centers for charge carriers. However, from 900 to 1200 °C, there was an increase in resistivity with the smaller order (10^8). From 1200 to 1400 °C, the increase of resistance was in 10^{10} order suggesting that when sintering temperature was increased from 900 to 1200 °C, the number of micropores such as isolated and closed pores within grains dominated [28]. After 1200 °C, the number of macropores such as intragranular pores increased and causing a rise in resistivity [10].

Conclusion

Polycrystalline, single-phase cobalt nickel ferrite ($Co_{0.5}Ni_{0.5}Fe_2O_4$) was successfully produced through high energy ball milling followed by a sintering process. Single-sample sintering of $Co_{0.5}Ni_{0.5}Fe_2O_4$ shows the thermal history and its effect can be observed in the fluctuation of lattice strain and crystallite size. The microstructural evolution showed three stages of grain growth which are initial, intermediate and final

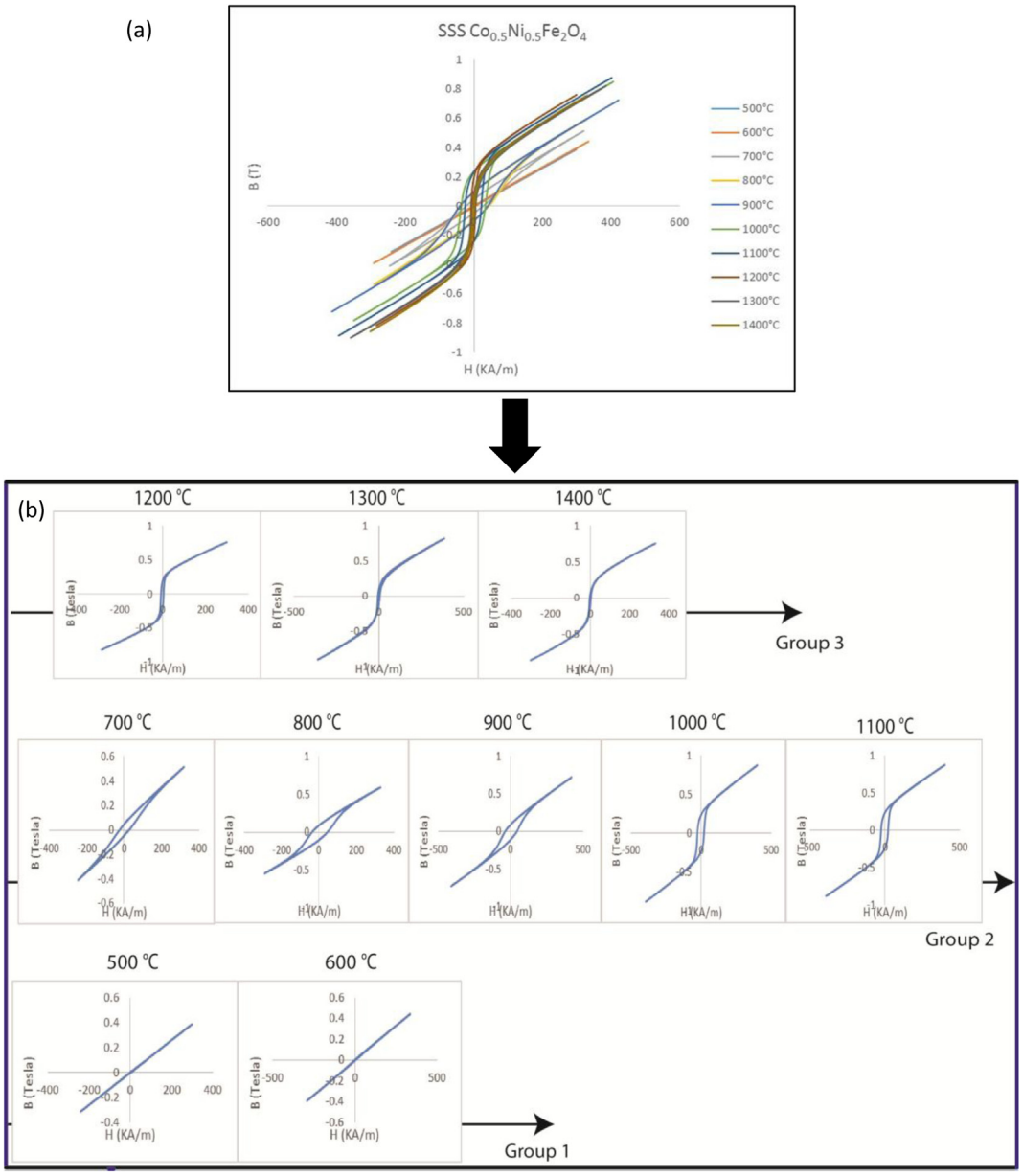

Fig. 6. B-H hysteresis graph of SSS $Co_{0.5}Zn_{0.5}Fe_2O_4$ for (a) combined graph for different sintering temperatures; (b) three different shape groups.

Table 2
B-H properties analysis of SSS CoNi samples sintered from 500 °C until 1400 °C.

Sintering temperature (°C)	Average grain size (nm)	H_c (KOe)	B_s (emu/g)	BH_{max}	Curie temperature (°C)
500	48.25	0.064	2.38	0.00	0
600	71.93	0.005	5.31	0.00	0
700	83.65	0.313	23.98	0.04	0
800	104.86	0.515	39.46	0.14	430
900	186.75	0.55	44.77	0.19	650
1000	297.85	0.461	64.05	0.3	540
1100	374.79	0.295	91.09	0.28	570
1200	964.73	0.08	101.37	0.06	580
1300	6762.66	0.042	109.78	0.03	590
1400	11215.91	0.026	99.07	0.00	480

stage. Higher sintering temperature at 1400 °C has caused an abnormal grain growth which greatly affects the magnetic and resistivity properties. The activation energies of each grain growth were also

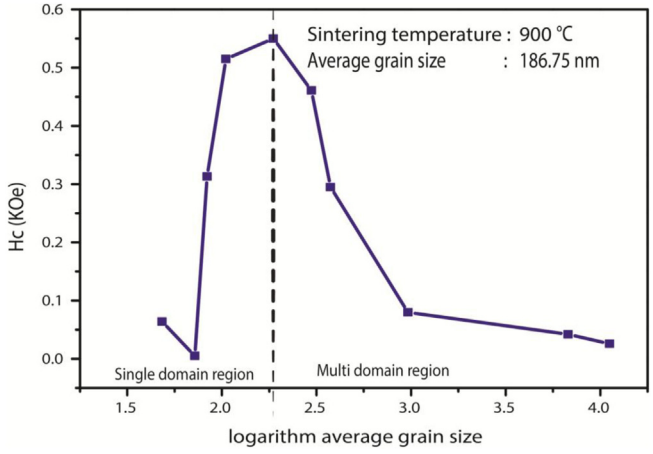

Fig. 7. Coercivity versus logarithm average grain size of SSS $Co_{0.5}Ni_{0.5}Fe_2O_4$.

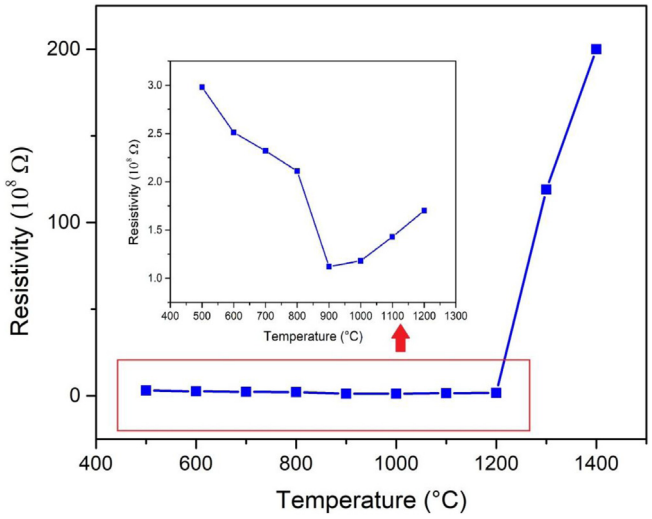

Fig. 8. Resistivity versus sintering temperature of SSS $Co_{0.5}Ni_{0.5}Fe_2O_4$.

increasing with the microstructural changes. The magnetic properties were divided into three groups based on the distinctive shapes of the hysteresis loops. These magnetic groups are correlated to the magnetic phase which are paramagnetic, superparamagnetic and ferromagnetic behavior of $Co_{0.5}Ni_{0.5}Fe_2O_4$. A transition of single domain to a multi-domain region was found with sintering at 900 °C with grain size of 186 nm. The resistivity property was greatly influence by the microstructural changes.

Author statement

We declare that it has not been published, neither has it been concurrently submitted for publication in another journal. It is based on our original work conducted under careful experimental work.

Declaration of Competing Interest

The authors declare that they have no known competing financial interests or personal relationships that could have appeared to influence the work reported in this paper.

Acknowledgement

The authors are thankful to Universiti Putra Malaysia for research facilities and financial support of Putra MUDA Research Grant (Vot: 9545400) and Tubitak research grant (project no.: 218M341) from The Scientific And Technological Research Council Of Turkey (TUBITAK), Turkey.

Appendix A. Supplementary data

Supplementary data to this article can be found online at https://doi.org/10.1016/j.rinp.2019.102683.

References

[1] Valenzuela R. Magnetic ceramics. New York: Cambridge University Press; 1994.
[2] Hajalilou A, Hashim M, Ebrahimi-Kahrizsangi R, Kamari HM. Influence of evolving microstructure on electrical and magnetic characteristics in mechanically synthesized polycrystalline Ni-ferrite nanoparticles. J Alloys Compd 2015;633:306–16. https://doi.org/10.1016/j.jallcom.2015.02.061.
[3] Waje SB, Hashim M, Wan Yusoff WD, Abbas Z. Sintering temperature dependence of room temperature magnetic and dielectric properties of $Co_{0.5}Zn_{0.5}Fe_2O_4$ prepared using mechanically alloyed nanoparticles. J Magn Magn Mater 2010;322:686–91. https://doi.org/10.1016/j.jmmm.2009.10.041.
[4] Xiang J, Chu Y, Shen X, Zhou G, Guo Y. Electrospinning preparation, characterization and magnetic properties of cobalt – nickel ferrite ($Co_{1-x}Ni_{(x)}Fe_2O_4$) nanofibers. J. Colloid Interface Sci. 2012;376:57–61. https://doi.org/10.1016/j.jcis.2012.02.068.
[5] Almessiere MA, Slimani Y, Sertkol M, Nawaz M, Sadaqat A, Baykal A, et al. Effect of Nb^{3+} substitution on the structural, magnetic, and optical properties of $Co_{0.5}Ni_{0.5}Fe_2O_4$ nanoparticles. Nanomaterials 2019;9.. https://doi.org/10.3390/nano9030430.
[6] Vijaya Babu K, Satyanarayana G, Sailaja B, Santosh Kumar GV, Jalaiah K, Ravi M. Structural and magnetic properties of $Ni_{0.8}M_{0.2}Fe_2O_4$ (M = Cu, Co) nano-crystalline ferrites. Results Phys 2018;9:55–62. https://doi.org/10.1016/j.rinp.2018.01.048.
[7] Verma KC, Goyal N, Singh M, Singh M, Kotnala RK. Hematite α-Fe_2O_3 induced magnetic and electrical behavior of $NiFe_2O_4$ and $CoFe_2O_4$ ferrite nanoparticles. Results Phys 2019;13:102212https://doi.org/10.1016/j.rinp.2019.102212.
[8] Bhujun B, Tan MTT, Shanmugam AS. Study of mixed ternary transition metal ferrites as potential electrodes for supercapacitor applications. Results Phys 2017;7:345–53. https://doi.org/10.1016/j.rinp.2016.04.010.
[9] Ismail I, Hashim M, Matori KA, Alias R, Hassan J. The transition from paramagnetic to ferromagnetic states as influenced by evolving microstructure of $Ni_{0.5}Zn_{0.5}Fe_2O_4$. J Supercond Nov Magn 2012;25. https://doi.org/10.1007/s10948-011-1201-x.
[10] Low ZH, Hashim M, Ismail I, Kanagesan S, Ezzad Shafie MS, Idris FM, et al. Development of Magnetic B-H Hysteresis Loops Through Stages of Microstructure Evolution of Bulk $BaFe_{12}O_{19}$. J Supercond Nov Magn 2015;28:3075–86. https://doi.org/10.1007/s10948-015-3099-1.
[11] Shafie MSE, Hashim M, Ismail I, Kanagesan S, Fadzidah MI, Idza IR, et al. Magnetic M-H loops family characteristics in the microstructure evolution of $BaFe_{12}O_{19}$. J Mater Sci Mater Electron 2014;25.. https://doi.org/10.1007/s10854-014-2090-0.
[12] Idza IR, Hashim M, Rodziah N, Ismayadi I, Norailiana AR. Influence of evolving microstructure on magnetic-hysteresis characteristics in polycrystalline nickel-zinc ferrite, $Ni_{0.3}Zn_{0.7}Fe_2O_4$. Mater Res Bull 2012:47. https://doi.org/10.1016/j.materresbull.2012.03.007.
[13] Ismayadi I, Hashim M, Khamirul AM, Alias R. The effect of milling time on $Ni_{0.5}Zn_{0.5}Fe_2O_4$ compositional evolution and particle size distribution. Am J Appl Sci 2009:6. https://doi.org/10.3844/ajassp.2009.1548.1552.
[14] Nazlan R, Hashim M, Abdullah NH, Ibrahim IR, Ismail I. Influence of milling time on the crystallization, morphology and magnetic properties of polycrystalline yttrium iron garnet. vol. 501. 2012. doi:10.4028/www.scientific.net/AMR.501.324.
[15] Ismail I, Hashim M, Amin Matori K, Alias R, Hassan J. Milling time and BPR dependence on permeability and losses of $Ni_{0.5}Zn_{0.5}Fe_2O_4$ synthesized via mechanical alloying process. J Magn Magn Mater 2011:323. https://doi.org/10.1016/j.jmmm.2011.01.002.
[16] Manju BG, Raji P. Synthesis and magnetic properties of nano-sized $Cu_{0.5}Ni_{0.5}Fe_2O_4$ via citrate and aloe vera: a comparative study. Ceram Int 2018;44:7329–33. https://doi.org/10.1016/j.ceramint.2018.01.201.
[17] Yadav RS, Kuřitka I, Vilcakova J, Havlica J, Masilko J, Kalina L, et al. Impact of grain size and structural changes on magnetic, dielectric, electrical, impedance and modulus spectroscopic characteristics of $CoFe_2O_4$ nanoparticles synthesized by honey mediated sol-gel combustion method. Adv Nat Sci Nanosci Nanotechnol 2017;8:45002. https://doi.org/10.1088/2043-6254/aa853a.
[18] Yamamoto H, Nissato Y. Magnetic properties of Co-Ni spinel ferrite fine particles with high coercivity prepared by the chemical coprecipitation method. IEEE Trans Magn 2002;38:3488–92. https://doi.org/10.1109/TMAG.2002.802717.
[19] Hankare PP, Sanadi KR, Garadkar KM, Patil DR, Mulla IS. Synthesis and characterization of nickel substituted cobalt ferrite nanoparticles by sol–gel auto-combustion method. J Alloys Compd 2013;553:383–8. https://doi.org/10.1016/j.jallcom.2012.11.181.
[20] Dippong T, Levei EA, Cadar O, Deac IG, Diamandescu L, Barbu-Tudoran L. Effect of nickel content on structural, morphological and magnetic properties of $Ni_xCo_{1-x}Fe_2O_4/SiO_2$ nanocomposites. J Alloys Compd 2019;786:330–40. https://doi.org/10.1016/j.jallcom.2019.01.363.
[21] Dippong T, Deac IG, Cadar O, Levei EA, Diamandescu L, Borodi G. Effect of Zn content on structural, morphological and magnetic behavior of $Zn_xCo_{1-x}Fe_2O_4/SiO_2$ nanocomposites. J Alloys Compd 2019;792:432–43. https://doi.org/10.1016/j.jallcom.2019.04.059.
[22] Goya GF, Rechenberg HR. Ionic disorder and Néel temperature in $ZnFe_2O_4$ nanoparticles. J Magn Magn Mater 1999;196–197:191–2. https://doi.org/10.1016/S0304-8853(98)00723-9.
[23] Sepelak V, Tkacova K, Boldyrev VV. Crystal structure refinement of the mechanically activated spinel-ferrite. Mater Sci Forum 1996;783:228–31. https://doi.org/10.4028/www.scientific.net/MSF.228-231.783.
[24] Low ZH, Chen SK, Ismail I, Tan KS, Liew JYC. Structural transformations of mechanically induced top-down approach $BaFe_{12}O_{19}$ nanoparticles synthesized from high crystallinity bulk materials. J Magn Magn Mater 2017;429:192–202. https://doi.org/10.1016/J.JMMM.2017.01.036.
[25] Mote V, Purushotham Y, Dole B. Williamson-Hall analysis in estimation of lattice strain in nanometer-sized ZnO particles. J Theor Appl Phys 2012;6:2–9. https://doi.org/10.1186/2251-7235-6-6.
[26] Ismail I, Hashim M, Ibrahim IR, Nazlan R, Mohd Idris F, Shafie SE, et al. Crystallinity and magnetic properties dependence on sintering temperature and soaking time of mechanically alloyed nanometer-grain $Ni_{0.5}Zn_{0.5}Fe_2O_4$. J Magn Magn Mater 2013;333.. https://doi.org/10.1016/j.jmmm.2012.12.047.
[27] Kang SJL. Sintering Densification, Grain Growth, and Microstructure. London, United Kingdom: Elsevier; 2005. doi: http://dx.doi.org/10.1016/B978-075066385-4/50009-1.
[28] Rahaman MN. Sintering of Ceramics. Boca Raton: CRC Press; 2007. doi:10.1201/b15869.
[29] Sameshima S, Higashi K, Hirata Y. Sintering and grain growth of rare-earth-doped ceria particles. J Ceram Process Res 2000;1:27–33.

[30] Ibrahim IR, Hashim M, Nazlan R, Ismail I, Kanagesan S, Wan Ab Rahman WN, et al. A comparative study of different sintering routes effects on evolving microstructure and B-H magnetic hysteresis in mechanically-alloyed Ni–Zn ferrite, $Ni_{0.3}Zn_{0.7}Fe_2O_4$. J Mater Sci Mater Electron 2014:26. https://doi.org/10.1007/s10854-014-2362-8.

[31] Ismail I, Hashim M, Kanagesan S, Ibrahim IR, Nazlan R, Wan Ab Rahman WN, et al. Evolving microstructure, magnetic properties and phase transition in a mechanically alloyed $Ni_{0.5}Zn_{0.5}Fe_2O_4$ single sample. J Magn Magn Mater 2014:351. https://doi.org/10.1016/j.jmmm.2013.09.041.

[32] Ibrahim IR, Hashim M, Nazlan R, Ismail I, Wan Ab Rahman WN, Abdullah NH, et al. Grouping trends of magnetic permeability components in their parallel evolution with microstructure in $Ni_{0.3}Zn_{0.7}Fe_2O_4$. J Magn Magn Mater 2014:355. https://doi.org/10.1016/j.jmmm.2013.12.024.

[33] Yaseneva P, Bowker M, Hutchings G. Structural and magnetic properties of Zn-substituted cobalt ferrites prepared by co-precipitation method. Phys Chem Chem Phys 2011;13:18609–14. https://doi.org/10.1039/c1cp21516g.

[34] Ismail I, Hashim M, Matori KA, Alias R, Hassan J. The transition from paramagnetic to ferromagnetic states as influenced by evolving microstructure of $Ni_{0.5}Zn_{0.5}Fe_2O_4$. J Supercond Nov Magn 2012;25:71–7. https://doi.org/10.1007/s10948-011-1201-x.

[35] Nazlan R, Hashim M, Ibrahim IR, Abdullah NH, Mohd Idris F, Ismayadi I, et al. Influence of Microstructural Evolution on the Magnetically Group Dominance in Polycrystalline $Y_3Fe_5O_{12}$ Multi-Samples. Mater Sci Forum 2016;846:366–74. https://doi.org/10.4028/www.scientific.net/MSF.846.366.

[36] Srinivasa Rao K, Ranga Nayakulu SV, Chaitanya Varma M, Choudary GSVRK, Rao KH. Controlled phase evolution and the occurrence of single domain $CoFe_2O_4$ nanoparticles synthesized by PVA assisted sol-gel method. J Magn Magn Mater 2018;451:602–8. https://doi.org/10.1016/j.jmmm.2017.11.069.

[37] Patta GR, Kumar VR, Rao KH, Veeraiah N. Synthesis and studies on magnetic properties of single-phase cobalt ferrite nanoparticles: influence of content of chelating agent. Appl Phys A 2019;125:187. https://doi.org/10.1007/s00339-019-2489-9.

[38] Kim T, Lim S, Hong J, Kwon SG, Okamoto J, Chen ZY, et al. Giant thermal hysteresis in Verwey transition of single domain Fe_3O_4 nanoparticles. Sci Rep 2018;8:5092. https://doi.org/10.1038/s41598-018-23456-6.

[39] Xu G, Zhang X, He W, Liu H, Li H, Boughton RI. Preparation of highly dispersed YAG nano-sized powder by co-precipitation method. Mater Lett 2006;60:962–5. https://doi.org/10.1016/j.matlet.2005.10.052.

[40] Shafi KVPM, Koltypin Y, Gedanken A, Prozorov R, Balogh J, Lendvai J, et al. Sonochemical Preparation of Nanosized Amorphous $NiFe_2O_4$ Particles. J Phys Chem B 2002;101:6409–14. https://doi.org/10.1021/jp970893q.